 doi:10.20944/preprints202107.0582.v1

Article

Module-Type Triboelectric Nanogenerators Capable of Harvesting Power from a Variety of Mechanical Energy Sources

Jaehee Shin [1], Sungho Ji [1], Jiyoung Yoon [2] and Jinhyoung Park [1,*]

[1] School of Mechatronics Engineering, Korea University of Technology & Education, Cheonan, Chungjeolro1600, South Korea; wogmlchs@koreatech.ac.kr (J.S); tjdghtmsk@koreatech.ac.kr (S.J)
[2] Safety System R&D Group, Korea Institute of Industrial Technology, 320 Techno sunhwan-ro, Yugamyeon, Daegu 42994, Dalseong-gun, Korea; gonji82@kitech.re.kr (J.Y)
* Correspondence: jhpark98@koreatech.ac.kr; Tel.: +82-41-560-1124

Abstract: In this study, we propose a module-type triboelectric nanogenerator (TENG) capable of harvesting power from a variety of mechanical energy sources. The potential energy and kinetic energy of water are used for the rotational motion of the generator module, and electricity is generated by the contact/separation generation mode between the two triboelectric surfaces inside the rotating TENG. Through the parametric design of the internal friction surface structure and mass ball, we optimized the output of the proposed structure. To magnify the power, experiments were conducted to optimize the electrical output of the series of TENG units. The electrical signal generated by the module-type TENG can be used as a sensor to recognize the strength and direction of various physical quantities, such as wind or earthquake vibrations.

Keywords: energy harvesting; triboelectric nanogenerators; vibration energy

1. Introduction

The various electronic devices that we use in our daily lives require power supplies. There are electronic devices that operate by using power wires, but there are also electronic devices that need continuous charging or require battery replacement, such as smartphones, Bluetooth earphones, flashlights, watches, etc. [1,2]. These electronic devices that use electricity and batteries as power sources provide a great deal of convenience in our daily lives. Presently, due to the evolution of technology, it is the era in which automobiles are also powered by electricity [3]. However, electricity has some limitations i.e., it is generated by power, which requires another energy source, such as fossil fuels resulting in the creation of environmental problems. To date, electricity has been generated through fossil fuel-based energy generation, which has led to climate problems [4]. Hence, we propose an environmentally friendly energy generation technique that employs technology that uses numerous everyday forms of triboelectricity as electric power [5]. This technology is called a triboelectric nanogenerator, and it can use the properties of electricity to harvest small amounts of electricity from the various forms of mechanical energy that occur around us, such as the simple contact or shaking of materials that have different properties [6]. Each material has different properties, but fundamentally, the atoms that make up the materials are composed of various configurations of positive and negative electrons. According to the triboelectric series, polarity occurs as electrons are gained and lost when there is contact between materials. Among materials with different properties, negatively and positively charged materials have the ability to easily take and give electrons, respectively. In the polarity that occurs during the process of material surfaces making contact, triboelectricity is generated [7–9]. Triboelectricity can be used not just for power generation but also for sensors. Triboelectric nanogenerators can be used as sensors because the amount of electricity that occurs during friction responds sensitively to the degree of external friction [10–13]. Triboelectric nanogenerator-based sensors are self-powered, and they can be used to measure various physical quantities [14]. By

 doi:10.20944/preprints202107.0582.v1

floating a circular triboelectric nanogenerator element in the ocean, it is possible to monitor the strength of waves [15–19], measure wind power, detect wind direction [20–23], and measure the amount of water falling from above [24–28]. In the future, self-powered triboelectric sensors will play an important role in obtaining various forms of data. In this study, a self-powered generator made from a cylindrical frame and a device that can be used as a sensor was manufactured in modular form so that the device could be easily placed in various environments. It was designed to carry a wide range of signals and high outputs when several devices were joined together rather than just a single device. According to the triboelectric series for multiple positively charged bodies, the difference in electrical potential can be determined by attaching aluminum to nitrile sheets. When a force of 3 to 7 Hz of frequency vibration was applied to the cylindrical frame, it moved vertically up and down. An experiment was conducted using this process to create contact and separation between the surfaces of the mass balls. The balls were made with copper inside them, and bump and dimple patterns were added to the balls to increase the contact area between the surfaces. The experiments were performed with Dragon Skin (D.S.) balls without copper, D.S. balls that included Cu wool, D.S.+ Cu wool balls that used the dimple pattern, and D.S.+ Cu wool balls that used the bump pattern to increase output.

2. Materials and Methods

2.1. Fabrication process of triboelectric nanogenerator (TENG) device and silicone rubber balls

Fig. 1a shows a schematic diagram of a TENG, which shows it to be in a state of dynamic behavior. The housing of the TENG was created by the fused deposition modeling (FDM) method using a 3D printer (DP203 3D WOX1, Sindoh). Poly Lactic Acid (PLA) was used as the building material. To check the effect of the design and experimental variables, the housing size was designed to have an outer diameter of 90 mm, an inner diameter of 80 mm, and a height of 105 mm. The angle formed with the floor was set at 0°, 30°, 60°, and 90°

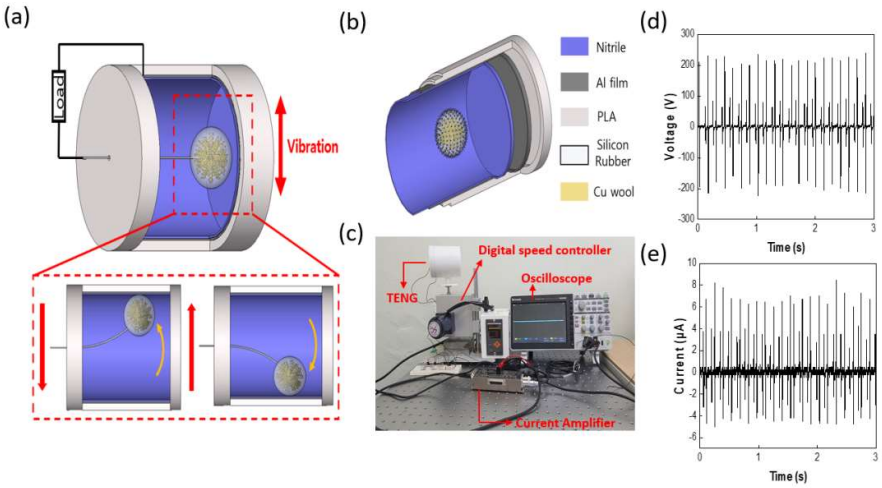

Figure 1. Triboelectric nanogenerator (TENG) schematic and experiment configuration: Diagrams showing (a) schematic and movement of TENG in a dynamic state; (b) material composition of TENG; (c) Photograph of the experiment configuration equipment, and plots showing; (d) the output voltage and (e) output current of TENG.

As shown in Fig. 1b, the interior housing of the TENG was covered with an electrode and a positively charged body in that order. An aluminum film was used as the electrode. The aluminum film, nitrile rubber, and paper were each used as positively charged bodies to analyze their effects on output. To create the ball that was used as the negatively

charged body, a magnetic bar was used to stir a 1:1 ratio of Part A (D.S. NV10) and Part B (curing agent) for 5 min. Copper wool electrode of 0.9 g was mixed in the properly stirred silicone rubber. Then, 17 g was poured into the master mold created using the FDM 3D printer and dried for approximately 6 h at room temperature (23°C). Once created, the composite was inserted into the TENG housing, and a normal single wire (outer diameter of 1.3 mm) was connected to the top plate of the housing to create a pendulum motion, as illustrated in Figure 1a.

2.2. TENG Device Assessment

To measure the output performance of the constructed TENG device, we used an oscilloscope (TBS 2072, Tektronix), voltage probe (P5100A, Tektronix), and current pre-amplifier (DLPCA-200, Femto), as shown in Fig. 1c. Additionally, an experiment was conducted in which a digital speed controller (subseries, SPG) was used to create a frequency of 3–7 Hz to apply pendulum motion to the TENG and calculate the optimal dynamic behavior data TENG device.

3. Results and Discussion

3.1. Preparation and Principle of the Potential energy-TriboElectric NanoGenerator (P-TENG)

A schematic of the TENG and its dynamic behavior are shown in Fig.1, and detailed information is provided in the experimental section. An FDM-based 3D printer using a PLA filament was used to construct the TENG housing, and the master mold was used to create the silicone rubber balls. The housing had an outer diameter of 90 mm and a height of 105 mm, and an inner diameter of 80 mm was covered with 1 mm of aluminum tape and 1 mm of nitrile rubber. This size is optimized to improve the output performance of the TENG. The silicone rubber balls that were made using the master mold were attached to the top plate of the housing using a normal single wire. It is located at approximately 70 mm for the purpose of creating a pendulum motion. As shown in Fig. 1b, the housing of the TENG consists of a PLA filament, an aluminum film, and nitrile rubber. For the silicone rubber ball, copper wool was mixed into the silicone rubber interior to improve the output. When a copper wool electrode is added to the interior of the silicone rubber, it is possible to obtain a higher dielectric constant and capacitance than that of the normal silicone rubber. As a result, it is possible to obtain a higher output value owing to the greater charge density that is transferred to the electrode [29–30]. Figs. 1d and e show the output voltage and current of the TENG. To perform the output tests, the input frequency of the digital speed controller was fixed at 7 Hz. As shown, the resulting output had a V_{oc} of 210 V and an I_{sc} of 9μA. The output electricity generation can be described as the charge transfer that occurs between the silicone rubber ball and the Al electrode during physical contact. Fig. 2 shows the mechanism of current generation via charge transfer when the TENG operates in the contact and separation modes. As shown in Fig. 2a, charge transfer does not occur in the completely separate initial state or the complete contact state because electrical neutrality is maintained. However, while the silicone rubber ball and the positively charged electrical body inside the housing are in the process of making contact or separation, charge transfer occurs to achieve electrical neutrality. During this time, the silicone rubber ball is charged as the negative pole, which has the quality of being able to obtain electrons easily, while the nitrile rubber and aluminum are charged as the positive pole, which has the property of being able to give away electrons easily. Due to the opposite polarity of the two materials, charge transfer occurs via an external circuit to achieve electrical neutrality, and current is generated. Fig. 2b is a modeling image for performing electromagnetic field analysis using the finite element analysis (FEA) technique of COMSOL Multiphysics.

Preprints (www.preprints.org) | NOT PEER-REVIEWED | Posted: 26 July 2021 doi:10.20944/preprints202107.0582.v1

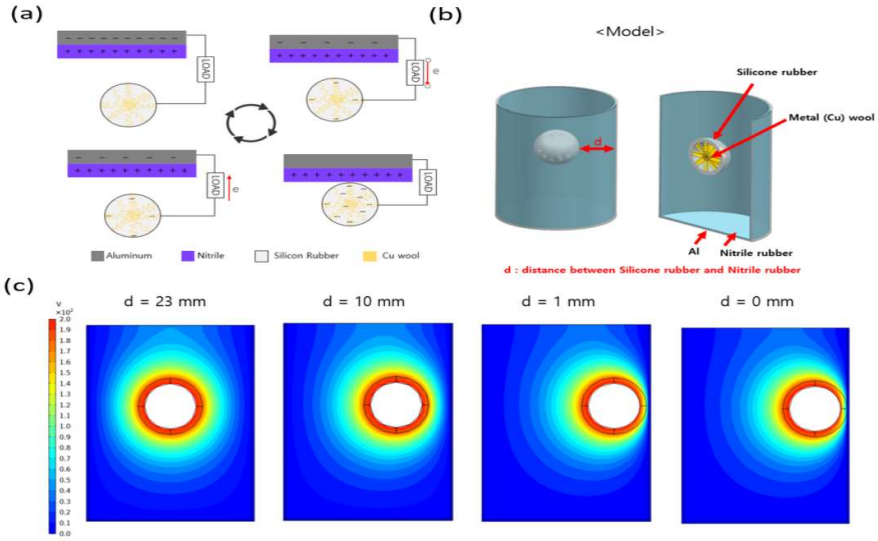

Figure 2. Contact and separation mode mechanism and COMSOL simulation of the P-TENG cylinder and Dragon Skin (D.S.) ball: (a) Schematic of Contact and Separation mode mechanism; (b) Diagram of showing modeling for simulation; (c) Gradient image depicting COMSOL simulation results.

To provide proof of the process described above, the results of an electrical field analysis using the COMSOL program are shown in Fig. 2c. It shows the changes in the electrical field according to the location of the silicone rubber ball. When the space (d) between the silicone rubber ball and the nitrile rubber is 1 mm, a potential difference occurs in the contact part, and a voltage of approximately 200 V is produced. This supports the claim that electron movement occurs when contact and separation occur between the silicone rubber ball and the interior of the housing.

3.2. Electrical Performance of the P-TENG

Fig. 3 shows the process of optimizing the electrical output characteristics when the TENG operates in the vertical contact separation mode. To obtain optimal data for the conditions under which the TENG device operates, experiments were performed using different frequencies. The experiments analyzed the voltage and current data that were produced as the input frequency of a digital speed controller were changed from 3 to 7 Hz. At a frequency of 3 Hz, an open-circuit voltage (Voc) of 10 V and an I_{sc} (short circuit current) of 3μA occurred. It was found that the voltage and current both increased linearly with frequency. Based on this, it is observed that the contact area increases, and the output voltage and current increase owing to the increase in the force acting on the silicone rubber ball and the motion energy as the frequency increases. At 4 Hz, there was a V_{oc} of 45 V and an I_{oc} of 4.5μA, and at 5 Hz, there was a V_{oc} of 150 V and an I_{sc} of 7μA. At 7 Hz, the V_{oc} and Isc were 250 V and 11μA, respectively. The experimental results show that the output values rose sharply, starting at 5 Hz. This occurred because as the frequency increased, the amplitude of the pendulum motion of the silicone rubber ball increased, and it was possible for the top and bottom surfaces of the TENG housing interior to make contact effectively. Owing to this effect, the output at 7 Hz improved by more than 200 V compared to that at 3 Hz, and the I_{sc} increased by more than 8μA. This was proven by the governing equation for a contact and separation-mode TENG, as shown below.

$$E = \frac{Q}{S\varepsilon_0\varepsilon_r} \quad (1)$$

Preprints (www.preprints.org) | NOT PEER-REVIEWED | Posted: 26 July 2021 doi:10.20944/preprints202107.0582.v1

$$V = -\frac{\sigma}{\varepsilon_0}\left(\frac{d}{\varepsilon_r} + x(t)\right) + \frac{\sigma x(t)}{\varepsilon_0} \tag{2}$$

$$I = -\frac{S\sigma\frac{d}{\varepsilon_r}v(t)}{(\frac{d}{\varepsilon_r} + x(t))^2} \tag{3}$$

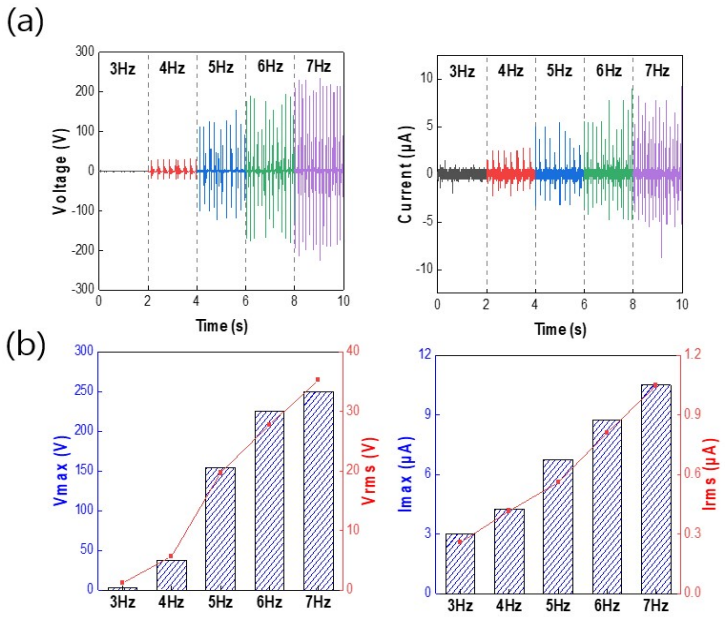

Figure 3. Plots depicting changes in output according to changes in frequency: (a-b) voltage and current occurring from 3 Hz to 7 Hz.

where, Q is the value of the transferred charges between the two electrodes, S is the dielectric area size, ε_0 is the vacuum permittivity, ε_r is the relative permittivity, σ is the friction charge surface density, $x(t)$ is the distance between two contact surfaces, t is the time, and d is the effective dielectric thickness. According to Eqs. 1, 2, and 3, when the frequency increases, the pendulum motion amplitude of the silicone rubber ball increases, and the contact area with the surface of the housing interior increases, which increases the wattage and current. As shown in Eqs. 1, 2, and 3, the electrical output performance of the TENG is significantly affected by the contact surface. Fig. 4 shows the normal form of the silicone rubber ball compared with those that had dimple and bump patterns newly applied to them in order to effectively increase their contact area. Fig. 4a shows a comparison of the four shapes of the silicone rubber balls. They are Only D.S. ball, D.S. +Cu Wool ball, Dimple ball, and Bump ball, in that order. Fig. 4b shows a graph that analyzes the changes in the voltage and current values according to the differences in the ball shape. As shown in Eqs. 1, 2, and 3, the electrical output performance of the TENG is significantly affected by the contact area. Fig. 4 shows the normally shaped silicone rubber ball compared with silicone rubber balls that have newly applied dimple and bump-shaped patterns to effectively increase their contact area.

Preprints (www.preprints.org) | NOT PEER-REVIEWED | Posted: 26 July 2021 doi:10.20944/preprints202107.0582.v1

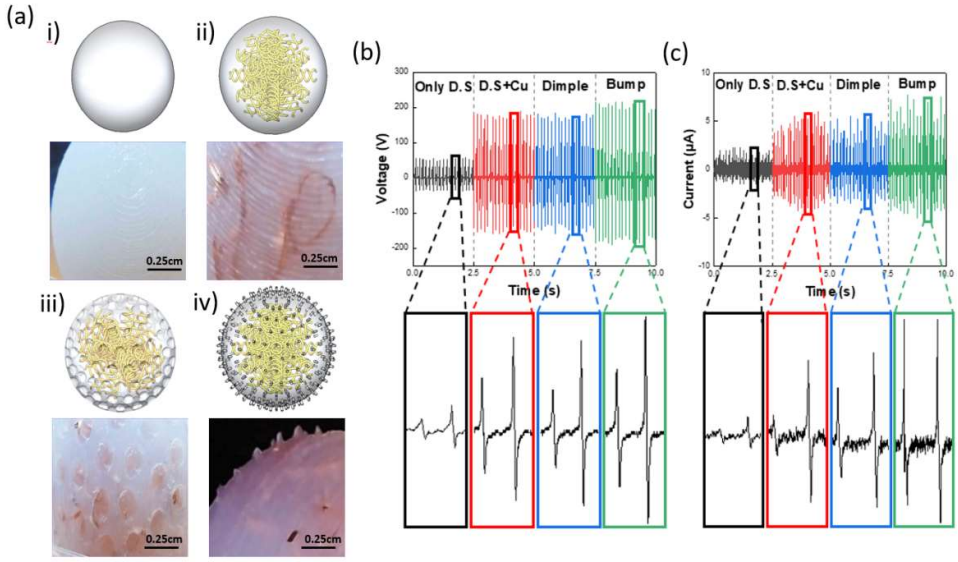

Figure 4. Changes in the output values according to the shape of the silicone rubber ball: (a) Pictorial representation and photographs of silicone rubber ball shapes i) the modeled shape and a 4x-magnification photograph of the silicone rubber surface of the ball made only of D.S., ii) the modeled shape and a 4x-magnification photograph of the silicone rubber surface of the ball made by mixing copper wool into the silicone rubber ball interior, iii) the modeled shape and a 4x-magnification photograph of the silicone rubber surface of the ball made by adding dimple shapes to the silicone rubber ball surface to change the contact area, and iv) the modeled shape and a 4x-magnification photograph of the silicone rubber surface of the ball made by adding bump-shaped wires to the surface of the silicon rubber ball to change the contact area; (b-c) Plots showing the voltage and current according to differences in the ball shape.

Fig. 4a shows a comparison of the 4 shapes of the silicone rubber balls. In order, they are: Only D.S. ball, D.S.+ Cu Wool ball, Dimple ball, and Bump ball. Fig. 4b is a graph that analyzes the changes in the voltage and current values according to differences in the ball shape. It is observed that the D.S.+ Cu wool ball, Dimple ball, and Bump ball did not show big changes in voltage and current, but the Only D.S. ball showed markedly lower voltage and current values. The reason for this is because the Only D.S. ball was the only one of the 4 shapes that operated in the single-electrode mode because it did not contain Cu wool that could act as an electrode. It is well known that single-electrode mode has lower electrical output performance than those of contact and separation mode. Therefore, it is observed that the Only D.S. ball obtained markedly lower output performance compared to the other ball shapes. Cu wool was added to achieve high capacitance and specific inductive capacity in order to receive a high charge density from the electrode so that a high output value could be produced. In the Dimple model, a dimple pattern was applied to the surface to increase the contact area, but when the model was used in practice, it was found that the generated contact area was slightly reduced, which had an adverse effect on the output value. It is expected that the contact area will increase and output performance will improve if an external force makes an extreme change to the shape of the ball. However, within the frequency range of the experiment, it is expected that there will be no major effect because the outer shape of the silicone rubber ball was not greatly changed. In the case of the bump shape, wire shapes with a diameter of 0.6 mm and a height of 1 mm performed the role of improving contact area when making contact with the surface of the housing interior. As shown in Fig. 4b, the highest output voltage and current were both obtained by the ball with bump shapes, which resulted in a V_{oc} of 210 V and an I_{sc} of 9μA.

Preprints (www.preprints.org) | NOT PEER-REVIEWED | Posted: 26 July 2021 doi:10.20944/preprints202107.0582.v1

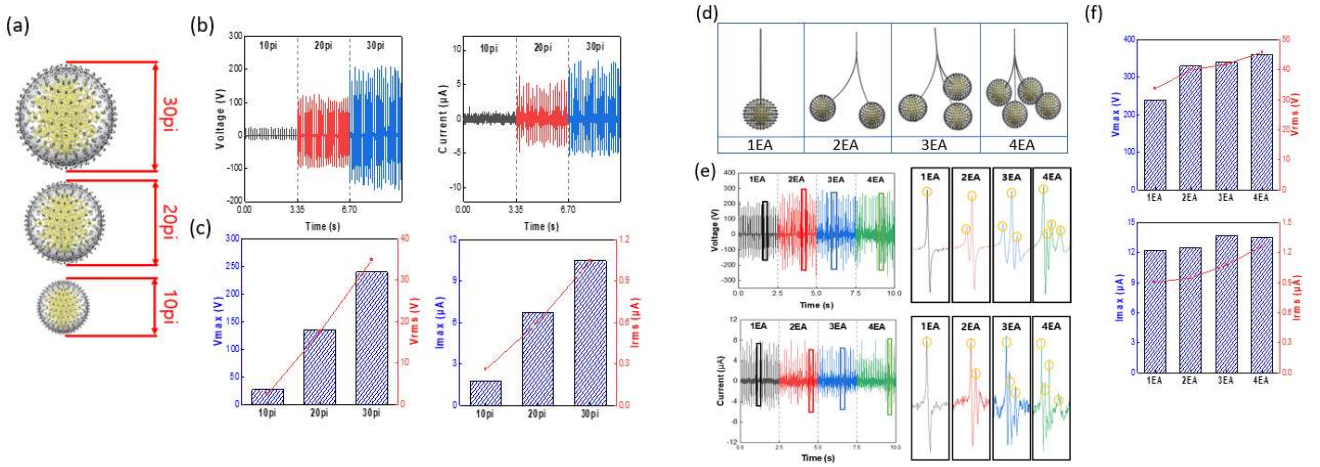

Figure 5. (a) Pictorial representation of various sizes of silicone rubber balls; (b-c) Plots depicting V_{max}, V_{rms}, I_{max}, I_{rms} according to size; (d) Schematic diagram comparing quantities of silicone rubber balls; (e-f) Plots of the voltage and current output waveform, and V_{max}, V_{rms}, I_{max}, I_{rms} according to quantity.

Fig. 5 compares and analyzes the changes in the output according to the size and quantity of dynamically behaving rubber balls in the TENG. First, to select the optimal size for the silicone rubber balls, the master mold was used to prepare 10 pi, 20 pi, and 30 pi balls, as shown in Fig. 5a. Their masses were 0.73 g, 5.44 g, and 15.8 g, respectively, and the masses of the copper wool within the silicone rubber balls were 0.2 g, 0.4 g, and 0.9 g, respectively. As shown in Figs. 5b and c, it was found that the voltage and current values increased as the sizes of the silicone rubber balls increased. This can be explained by Eqs. 1, 2, and 3. As the diameter increased, the friction charge surface density (σ) value increased along with the capacitance (C) value. Due to this, the 30pi silicon rubber ball created more charge transfer than the 10pi ball, and it was able to produce a large output value. From the actual measurement results, the 10 pi ball had a V_{oc} of around 30 V and an I_{sc} of 2μA, while the 30 pi ball had a V_{oc} of 200 V and an I_{sc} of 10μA. Fig. 5d shows a schematic diagram of silicone rubber balls connected in quantities of 1 to 4. The experiment conditions were set up so that the balls were fixed at 70 mm on the TENG housing interior and a frequency of 7 Hz was applied, just as in the experiments with a single silicone rubber ball. As the number of silicone rubber balls increased, there was no great difference in V_{max} or I_{max}. However, looking at the voltage and current waveforms, it can be seen that the density improved, and this is shown in Fig. 1e. Looking at the waveforms for a single silicone rubber ball, it can be seen that a single output was produced during the pendulum motion. Similarly, it can be seen that in the case of 2 balls, 2 outputs were produced for a single pendulum motion, while 3 and 4 balls produced 3 and 4 outputs, respectively. This helps to increase the V_{rms} and I_{rms} values because the density in the waveform is increased. From the data values, 1 ball had a V_{rms} of 33.71 V and an I_{rms} of 0.904μA, 2 balls had a V_{rms} of 39.954 V and an I_{rms} of 0.948μA, 3 balls had a V_{rms} of 41.869 V and an I_{rms} of 1.078μA, and 4 balls had a V_{rms} of 45.825 V and an I_{rms} of 1.27μA. Thus, it was found that the V_{rms} and I_{rms} values increased as the number of balls increased.

3.3. Properties on location and material

As shown in Fig. 6, the output at each angle of the P-TENG was analyzed. Experiments were performed to examine changes in the location of the TENG due to changes in the environment and changes in the state of the TENG due to the applied external force. As shown in Fig. 6a, the experiments were performed on frames built with angles of 0°, 30°, 60°, and 90°.

Preprints (www.preprints.org) | NOT PEER-REVIEWED | Posted: 26 July 2021 doi:10.20944/preprints202107.0582.v1

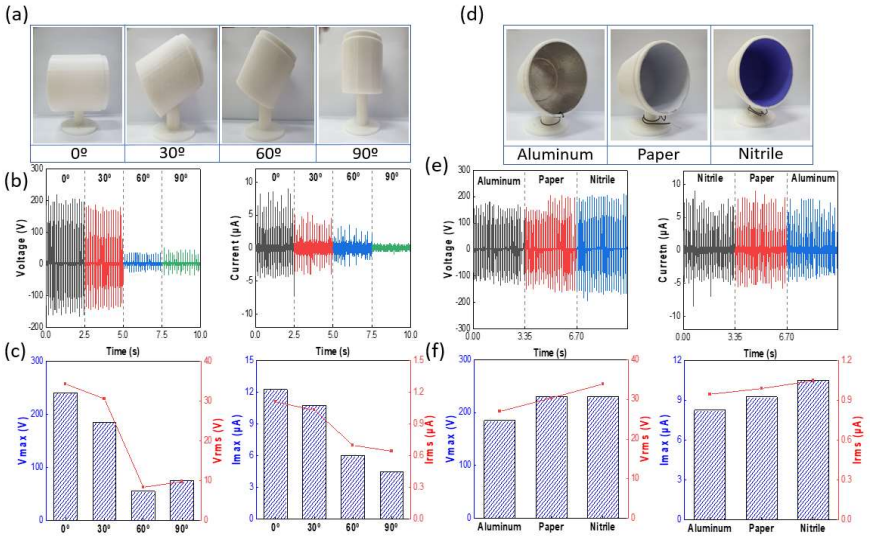

Figure 6. (a) Photographs showing the angles of the TENG cylinders; (b-c) Plots of V_{max}, V_{rms}, I_{max}, and I_{rms} according to the cylinder angles; (d) Photographs of the types of positively charged electrical bodies on the TENG interior surfaces, (e-f) Plots of V_{max}, V_{rms}, I_{max}, and I_{rms} values according to the type of positively charged electrical body.

In Figs. 6 b and c, the highest values (200 V and 9μA) were obtained at 0°. Conversely, the lowest output values (40 V, 1.5μA) were obtained at 90°. The output values were the lowest at 90° because at 0° it was possible to make effective contact and separation on both sides of the housing during the pendulum motion, while at 90°, a lower output value was obtained owing to a smaller contact area in comparison to that for 0°. Next, changes were made to the material of the positively charged body inside the cylinder. A comparative analysis was performed on the positively charged body, which follows the triboelectric series, using materials that are commonly encountered in daily life. Positively charged bodies were created using Al, Al+ nitrile, and Al+ paper, as shown in Fig. 6d. The most basic method for improving the output values of a triboelectric nanogenerator (TEG) is to increase the surface potential difference. To create a large surface potential difference, it is important to select a suitable positively charged body. In Figs. 6e and f, it is observed that nitrile had the highest output values among the three materials; therefore, Al+ nitrile was selected as the positively charged body of the P-TENG.

3.4. Application

As shown in Fig. 7, the output values found in the experiments were used to light LEDs that can operate at low power. To check the electrical power produced by the P-TENG, measurements were taken at a variable resistance of 1 MΩ to 1 GΩ, as shown in Fig. 7a. As the resistance increased, the voltage tended to increase, and the current decreased. The results of calculating the output power values for each external resistance value showed that the maximum power value was 460 μW at 100 MΩ. As shown in Fig. 7b, a bridge rectifier was used to assess the charging characteristics of the equipment, and the AC signal was converted into a DC signal. The capacitors used in the charging tests had the following capacitance levels: 0.82, 1, 1.5, 2.2, 3.3, 4.7, and 1nF. Fig. 7c shows a graph of the charging curve resulting from the use of a variety of capacitors under the same input conditions. 2.5 seconds were required to charge the 10nF capacitor to 14 V. The charged capacitors were used to turn on the LEDs that were connected to the output terminal, and the capacitors were discharged again.

Preprints (www.preprints.org) | NOT PEER-REVIEWED | Posted: 26 July 2021 doi:10.20944/preprints202107.0582.v1

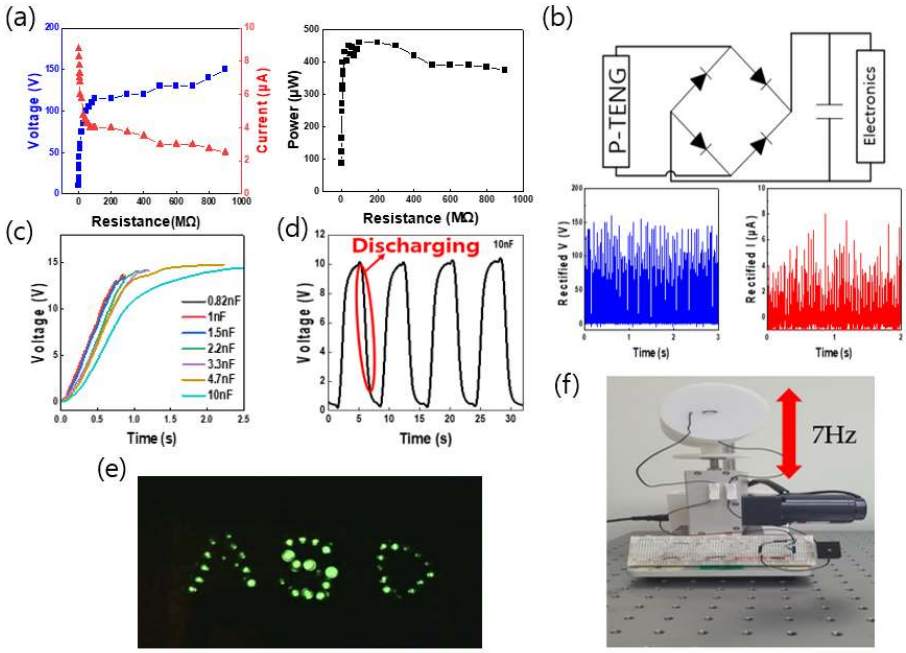

Figure 7. Application: (a) Plots depicting the influence of the load resistance on the P-TENG; (b) Rectification circuit diagram and rectification waveform of LED and capacitor; (c) Plot depicting the use of capacitors with different capacitance values (0.82, 1, 1.5, 2.2, 3.3, 4.7, and 10nF); (d) Plot of the curve of charge/discharge when 2 LEDs were connected; (e) Image of "ASD" pattern LED by the P-TENG; (f) Photograph of the digital speed controller and electrical circuit configuration.

Fig. 7d is a graph of the charge/discharge curve. To verify the performance of the P-TENG as an actual power source, a digital speed controller and an LED electric circuit were set up, and Fig. 7e shows the 40 LED lights.

5. Conclusion

Summarily, this study proposes and implements a P-TENG, which is a pendulum motion-based TENG that effectively collects the potential energy of a ball. To improve the generation performance, a copper wool electrode was inserted into the silicone rubber ball, thereby increasing the capacitance and achieving a higher output. Additionally, the dynamic behavior of the P-TENG was analyzed, and the design variables that affected the output were identified. The shape, size, and quantity of the silicone rubber ball significantly affected the contact area with the interior surface of the housing during dynamic behavior. To effectively improve the contact area, four new silicone rubber ball shapes (Only D.S. ball, D.S. +Cu Wool ball, Dimple ball, and Bump ball) were proposed, and it was found that the bump ball provided the highest generation performance. Additionally, it was found that the generation performance increased as the size and quantity of balls increased, and this is believed to be due to the increase in friction surface charge density and capacitance. Finally, the P-TENG device was used as a power source to light 40 LEDs and power commercial electronic products, which proved that the kinetic energy created by the potential energy of the ball can be effectively harvested as electrical energy. Varying output values can be produced when the angles are assigned to the TENG, and its shape status changes for each angle. By using these output values, it is possible to create a monitoring sensor that can detect the functional status and deformation states without directly checking the status. Therefore, the results of this study may be used for wind volume and wind speed measurement sensors in the future. This is expected to have two effects because a TENG can be used in a variety of situations as a module type.

Author Contributions: Conceptualization, methodology, writing-original draft, writing—review and editing, J.S. and S.J.; Simulation software, writing—review and editing, J.Y.; Validation, resources, writing—review and editing, J.P. All authors have read and agreed to the published version of the manuscript.

Funding: This work was supported by the National Research Foundation of Korea (NRF) grant funded by the Korea government (MSIT) [2018R1D1A1B07040446], the Korea Institute of Industrial Technology (KITECH) under the "AI platform for vision systems and applications Project" [JA210002], and Korea Institute for Advancement of Technology(KIAT) grant funded by the Korea Government(MOTIE) [P0008458].

Acknowledgments: We would like to thank the Korea University of Technology and Education Common Equipment Center for the use of their Scanning Electron Microscope.

Conflicts of Interest: The authors declare no conflict of interest.

References

1. Ku, M.-L.; Li, W.; Chen, Y.; Ray Liu, K. Advances in energy harvesting communications: Past, present, and future challenges. *IEEE Commun. Surv. Tutor.* **2015**, *18*, *1384–1412*. [Crossref].
2. Pu, X.; Hu, W.; Wang, Z.L. Toward wearable self-charging power systems: The integration of energy-harvesting and storage devices. *Small* **2018**, *14*. [Crossref]. [PubMed].
3. Hanifah, R.A.; Toha, S.F.; Ahmad, S. Electric vehicle battery modelling and performance comparison in relation to range anxiety. *Procedia Comput. Sci.* **2015**, *76*, 250–256. [Crossref] .
4. Martins, F.; Felgueiras, C.; Smitkova, M.; Caetano, N. Analysis of fossil fuel energy consumption and environmental impacts in European countries. *Energies* **2019**, *12*, 964. [Crossref] .
5. Fan, F.-R.; Tian, Z.-Q.; Lin Wang, Z.L. Flexible triboelectric generator. *Nano Energy* **2012**, *1*, 328–334. [Crossref] .
6. Zou, H.-X.; Zhao, L.-C.; Gao, Q.-H.; Zuo, L.; Liu, F.-R.; Tan, T.; Wei, K.; Zhang, W. Mechanical modulations for enhancing energy harvesting: Principles, methods and applications. *Appl. Energy* **2019**, *255*. [Crossref].
7. Kim, W.; Bhatia, D.; Jeong, S.; Choi, D. Mechanical energy conversion systems for triboelectric nanogenerators: Kinematic and vibrational designs. *Nano Energy* **2019**, *56*, 307–321. [Crossref].
8. Wang, Z.L.; Chen, J.; Lin, L. Progress in triboelectric nanogenerators as a new energy technology and self-powered sensors. *Energy Environ. Sci.* **2015**, *8*, 2250–2282. [Crossref].
9. Wu, C.; Wang, A.C.; Ding, W.; Guo, H.; Wang, Z.L. Triboelectric nanogenerator: A foundation of the energy for the new era. *Adv. Energy Mater.* **2019**, *9*. [Crossref].
10. Du, T.; Zuo, X.; Dong, F.; Li, S.; Mtui, A.E.; Zou, Y.; Zhang, P.; Zhao, J.; Zhang, Y.; Sun, P.; Xu, M. A self-powered and highly accurate vibration sensor based on bouncing-ball triboelectric nanogenerator for intelligent ship machinery monitoring. *Micromachines* **2021**, *12*, 218. [Crossref]. [PubMed].
11. Pu, X.; Guo, H.; Tang, Q.; Chen, J.; Feng, L.; Liu, G.; Wang, X.; Xi, Y.; Hu, C.; Wang, Z.L. Rotation sensing and gesture control of a robot joint via triboelectric quantization sensor. *Nano Energy* **2018**, *54*, 453–460. [Crossref].
12. Li, R.; Wei, X.; Xu, J.; Chen, J.; Li, B.; Wu, Z.; Wang, Z. Smart wearable sensors based on triboelectric nanogenerator for personal healthcare monitoring. *Micromachines* **2021**, *12*, 352. [Crossref]. [PubMed].
13. Hwang, H.J.; Lee, Y.; Lee, C.; Nam, Y.; Park, J.; Choi, D.; Kim, D. Mesoporous highly-deformable composite polymer for a gapless triboelectric nanogenerator via a one-step metal oxidation process. *Micromachines* **2018**, *9*, 656. [Crossref]. [PubMed]
14. Gao, Q.; Cheng, T.; Wang, Z.L. Triboelectric mechanical sensors—progress and prospects. *Extreme Mech. Lett.* **2021**, *42*. [Crossref].
15. Zhang, S.L.; Xu, M.; Zhang, C.; Wang, Y.-C.; Zou, H.; He, X.; Wang, Z.; Wang, Z.L. Rationally designed sea snake structure based triboelectric nanogenerators for effectively and efficiently harvesting ocean wave energy with minimized water screening effect. *Nano Energy* **2018**, *48*, 421–429. [Crossref].
16. Xiao, T.X.; Liang, X.; Jiang, T.; Xu, L.; Shao, J.J.; Nie, J.H.; Bai, Y.; Zhong, W.; Wang, Z.L. Spherical triboelectric nanogenerators based on spring-assisted multilayered structure for efficient water wave energy harvesting. *Adv. Funct. Mater.* **2018**, *28*. [Crossref].
17. Lin, Z.; Zhang, B.; Guo, H.; Wu, Z.; Zou, H.; Yang, J.; Wang, Z.L. Super-robust and frequency-multiplied triboelectric nanogenerator for efficient harvesting water and wind energy. *Nano Energy* **2019**, *64*. [Crossref].
18. Lee, K.; Lee, J.-W.; Kim, K.; Yoo, D.; Kim, D.S.; Hwang, W.; Song, I.; Sim, J. A spherical hybrid triboelectric nanogenerator for enhanced water wave energy harvesting. *Micromachines* **2018**, *9*, 598. [Crossref]. [PubMed].
19. Wang, X.; Niu, S.; Yin, Y.; Yi, F.; You, Z.; Wang, Z.L. Triboelectric nanogenerator based on fully enclosed rolling spherical structure for harvesting low-frequency water wave energy. *Adv. Energy Mater.* **2015**, *5*. [Crossref].
20. Park, J.; Han, M.; Kim, G.; Jung, Y.; Cho, H. Tree-wrapped triboelectric generator for harvesting wind energy. *J. Nanosci. Nanotechnol.* **2020**, *20*, 239–244. [Crossref]. [PubMed].
21. Bae, J.; Lee, J.; Kim, S.; Ha, J.; Lee, B.S.; Park, Y.; Choong, C.; Kim, J.B.; Wang, Z.L.; Kim, H.Y.; Park, J.J.; Chung, U.I. Flutter-driven triboelectrification for harvesting wind energy. *Nat. Commun.* **2014**, *5*, 4929. [Crossref]. [PubMed].

22. Win Zaw, N.Y.W.; Roh, H.; Kim, I.; Goh, T.S.; Kim, D. Omnidirectional triboelectric nanogenerator operated by weak wind towards a self-powered anemoscope. *Micromachines* **2020**, *11*, 414. [Crossref]. [PubMed].
23. Xia, Y.; Tian, Y.; Zhang, L.; Ma, Z.; Dai, H.; Meng, B.; Peng, Z. An optimized flutter-driven triboelectric nanogenerator with a low cut-in wind speed. *Micromachines* **2021**, *12*, 366. [Crossref]. [PubMed].
24. Kwon, S.-H.; Park, J.; Kim, W.K.; Yang, Y.; Lee, E.; Han, C.J.; Park, S.Y.; Lee, J.; Kim, Y.S. An effective energy harvesting method from a natural water motion active transducer. *Energy Environ. Sci.* **2014**, *7*, 3279–3283. [Crossref].
25. Chatterjee, S.; Saha, S.; Barman, S.R.; Khan, I.; Pao, Y.-P.; Lee, S.; Choi, D.; Lin, Z. Enhanced sensing performance of triboelectric nanosensors by solid–liquid contact electrification. *Nano Energy* **2020**, *77*. [Crossref].
26. Kim, T.; Chung, J.; Kim, D.Y.; Moon, J.H.; Lee, S.; Cho, M.; Lee, S.H.; Lee, S. Design and optimization of rotating triboelectric nanogenerator by water electrification and inertia. *Nano Energy* **2016**, *27*, 340–351. [Crossref].
27. Chung, S.-H.; Chung, J.; Kim, B.; Kim, S.; Lee, S. Screw pump-type water triboelectric nanogenerator for active water flow control. *Adv. Eng. Mater.* **2021**, *23*. [Crossref]. [PubMed].
28. Kim, T.; Kim, D.Y.; Yun, J.; Kim, B.; Lee, S.H.; Kim, D.; Lee, S. Direct-current triboelectric nanogenerator via water electrification and phase control. *Nano Energy* **2018**, *52*, 95–104. [Crossref].
29. Kim, J.; Cho, H.; Han, M.; Jung, Y.; Kwak, S.S.; Yoon, H.J.; Park, B.; Kim, H.; Kim, H.; Park, J.; Kim, S. Ultrahigh power output from triboelectric nanogenerator based on serrated electrode via spark discharge. *Adv. Energy Mater.* **2020**, *10*. [Crossref].
30. Park, J.; Cho, H.; Lee, Y.-S. Enhancing the triboelectric nanogenerator output by micro plasma generation in a micro-cracked surface structure. *Appl. Sci.* **2021**, *11*, 4262. [Crossref].